

A Nonisolated Wide Input Series Resonant Converter for Automotive LED Lighting System

V. K. Satyakar Veeramallu , *Member, IEEE*, S. Porpandiselvi , *Member, IEEE*,
and B. L. Narasimharaju , *Senior Member, IEEE*

Abstract—In this article, a reconfigurable nonisolated buck–boost (BB) integrated full-bridge series resonant converter (FB–SRC) based light emitting diode (LED) driver is proposed for wide input voltage automotive lighting applications. The proposed LED driver is derived by the integration of BB operation with FBSRC. It can be reconfigured into three different resonant converter topologies such as BB integrated FBSRC, BB integrated half-bridge series resonant converter (BB–HBSRC), and conventional HBSRC and, hence, produces three levels of voltage gains. By transformation from one topology to other based on the input voltage range and with asymmetrical pulsewidth modulation control, it can operate for wide input voltage range while maintaining the soft switching. The main advantages of the proposed configuration are smooth transformation into three different topologies without any additional switching devices, no topological transitions within a switching cycle in steady state, use of simple proportional–integral controller, soft switching, and wider voltage gain with buck/boost operation. In addition, dimming control is also achieved using pulsewidth modulation technique. Detailed theoretical analysis of the proposed converter is presented. To verify the analysis and performance, a prototype of 22.7 W, 22.5 V LED driver is designed, simulated, and tested for a wide input voltage range of 18 to 120 V.

Index Terms—Light emitting diode (LED), series resonant converter (SRC), wide gain, wide input.

I. INTRODUCTION

WITH effective utilization of lighting energy, more energy can be saved. In this perspective, lighting technology in various fields is modernized with light emitting diodes (LEDs) due to their enormous advantages like high efficiency, low maintenance, long life, dynamic response, etc. The LED lights are driven and, thus, regulated from LED drivers. Improved performance can be achieved from LEDs with an optimized design of LED drivers.

A battery of 12/24 V in automotive applications may vary up to 64 V during transients and can be even more [1], [2]. Further, there are different battery voltage systems available in the automotive system. Hence, there is a requirement of

LED drivers that can operate for wide input voltage ranges. There are few LED drivers [3]–[10] available with a wide input voltage range. LED drivers [3]–[7] are hard switched and, hence, have limitations like reduced power density, increased switching losses, and limited operating voltage range. The complex and costlier technologies like CMOS and BCDLite are employed in [3], [4], [6], and [8]–[10].

Indeed, there are many wide input converters developed for photovoltaic (PV), fuel cell applications, etc. High gain boost dc–dc converters [11], [12] are employed for wide input range fuel cell applications. An accurate adaptive constant on-time control scheme is used in [13] to improve the stability and performance under wide input/output voltage range applications. However, these converters are hard switched. Soft switched converters become popular as they are compact in size with high efficiency. An isolated buck–boost (BB) converter with a hybrid three-level full-bridge (FB) primary side circuit is used in [14] to achieve wider voltage gain regulation. Resonant converter (RC) with asymmetrical pulsewidth modulation (APWM) for voltage doubler rectifier is reported in [15] for wide input PV applications.

RCs have become popular due to their soft switching capability, high power density, etc. A multilevel LCC RC with more control flexibility [16] and LLC RCs with two split branches and variable magnetizing inductance [17], [18] are presented; however, two transformers are employed, which increases the size and cost. A double pulse duty cycle modulation that boosts the low input voltage and provides wide voltage regulation is reported for dc microgrid applications [19]. Several authors have developed reconfigurable converters [20]–[25] to achieve wide voltage gain with soft switching by modifying the LLC RCs with respect to the configuration or modulation or both. A hybrid control with frequency modulation (FM) and phase shift modulation (PSM) is employed in [20]. In [21] and [22], the diode bridge rectifier is replaced with semiactive rectifier. In [23] and [24], bidirectional switches are placed at the secondary side resonant tank and primary side, respectively. The dual bridge LLC RC [24] is a combination of half-bridge (HB) and FB RCs, where the voltage is regulated by the transition between HB and FB with respective time durations in one cycle. A series resonant converter (SRC) that provides four configurable operation states depending on input and output voltage levels [25] is reported for grid-connected PV systems. Boost or BB integrated RCs have become popular as they can produce a wide gain, thus suitable for wide input applications [26]–[30]. In [26], interleaved boost

Manuscript received March 23, 2020; revised July 21, 2020 and September 13, 2020; accepted October 3, 2020. Date of publication October 20, 2020; date of current version January 22, 2021. Recommended for publication by Associate Editor W. Huang. (*Corresponding author: V. K. Satyakar Veeramallu.*)

The authors are with the Electrical Engineering, National Institute of Technology, Warangal 506004, India (e-mail: vvk.satyakar@student.nitw.ac.in; selvi@nitw.ac.in; blnraju@nitw.ac.in).

Color versions of one or more of the figures in this article are available online at <http://ieeexplore.ieee.org>.

Digital Object Identifier 10.1109/TPEL.2020.3032159

operation is integrated with FB LLC RC and simple pulsewidth modulation (PWM) control is employed. But there is a high startup current in these converters due to the boost operation that results in high switching stress across the devices. Thus, BB integrated RCs are gaining importance as they have a small startup current due to the characteristics of BB operation [27]. In [27], BB operation is integrated with HB LLC RC where both the primary side and secondary side switches are modulated to operate for wide input voltage applications without affecting the zero voltage switching (ZVS) across devices. In [28], BB operation is integrated with HB LCC RC, where hybrid control combination of PWM and FM controls are employed. In [29], a four-switch noninverting BB operation is integrated with FB LLC RC. In [30], BB operation is integrated with dual bridge LLC RC. PSM control is employed for adjusting the gains and FM control is employed to regulate the output voltage. All these converters are of isolated type. Some of them have control complexity either due to hybrid control or due to transition from one configuration to another in each cycle. Some topologies have increased component count that increases the conduction losses. Some topologies require additional gate driver circuits due to the replacement of switches with diodes.

For low power applications, a nonisolated SRC is a better choice due to its easier implementation, reduced cost, and size. Thereby, in this article, a reconfigurable nonisolated BB integrated full-bridge series resonant converter (FBSRC) based LED driver is proposed for automotive LED lighting applications with wide input voltage variations. By proper switch configurations, it can be reconfigured as BB integrated FB SRC (BB-FBSRC), BB integrated half-bridge series resonant converter (BB-HBSRC), and conventional HBSRC. Thus, when compared with conventional HBSRC, it can produce three levels of gain viz., four times the gain with BB-FBSRC configuration, two times the gain with BB-HBSRC configuration, and the same gain with HBSRC configuration. By transformation from one topology to other based on the input voltage range and with APWM control, the proposed configuration can operate for wide input voltage range while maintaining soft switching. As LED load is constant, and automotive applications have wide input voltage variations, the proposed configuration is well suitable as an LED driver in automotive applications. PWM dimming is used for illumination control that controls the average LED current. Description of the proposed configuration and its working principle are presented in Section II. Analysis of the converter is presented in Section III. Design aspects of the converter are discussed in Section IV. Simulation and experimental results are presented in Section V. Efficiency analysis and comparative study are carried out in Section VI, and Section VII concludes the article.

II. PROPOSED CONFIGURATION AND WORKING PRINCIPLE

A. Description of Proposed Topology

The circuit diagram of the proposed LED driver is shown in Fig. 1, which consists of a synchronous BB converter integrated with FBSRC. S_1 to S_4 are the four MOSFET switches with body diodes and snubber capacitors. D_{R1} to D_{R4} are the diodes that constitute the diode bridge rectifier. L_r and C_r are the series

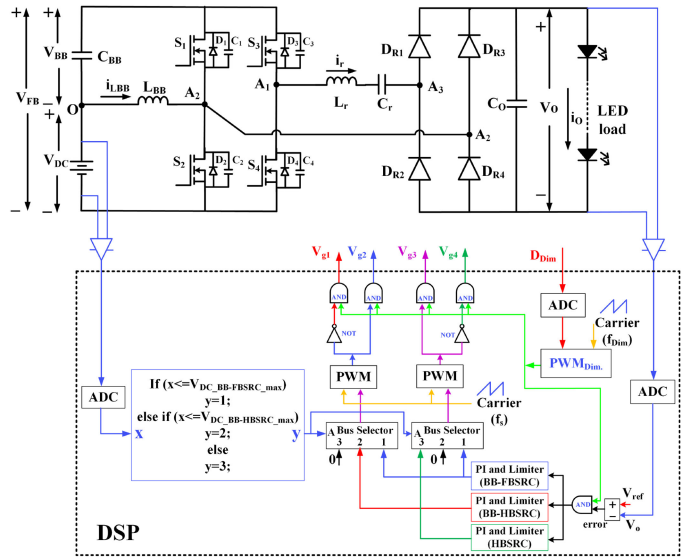


Fig. 1. Proposed wide input voltage LED driver.

resonant elements. C_o is the output capacitor. C_{BB} , S_1 , S_2 , and inductor L_{BB} are the elements of integrated synchronous BB converter. V_{dc} , V_{BB} , and $i_{L_{BB}}$ are the input, output voltages, and inductor current corresponding to the BB operation. V_{FB} is the input voltage applied to the SRC and i_r is the resonant current. V_o and I_o are, respectively, the LED voltage and current.

B. Different Reconfigurations

In order to operate for wide input voltage range, the input voltage and switches of FB converter are effectively utilized in the proposed configuration. The two switches S_1 and S_2 in the FB RC are also shared for BB operation. Hence, the proposed configuration can be reconfigured into three different RC topologies based on the input voltage ranges. The first configuration is BB-FBSRC topology as shown in Fig. 2(a), where BB operation is integrated with FBSRC. Thus, with the voltage $V_{FB} = V_{dc} + V_{BB}$, BB-FBSRC produces four times the voltage gain compared to conventional HBSRC. The second configuration is BB-HBSRC topology, which is obtained by continuously maintaining switch S_3 in OFF state and switch S_4 in ON state as shown in Fig. 2(b), where BB operation is integrated with HBSRC. Thus, with the voltage $V_{FB} = V_{dc} + V_{BB}$, BB-HBSRC produces two times the voltage gain compared with conventional HBSRC. The third configuration is conventional HBSRC topology, which is obtained by continuously maintaining switch S_1 in ON state and switch S_2 in OFF state as shown in Fig. 2(c), where the voltage $V_{FB} = V_{dc}$. Thus, the three levels of voltage gains obtained are well utilized for operating under wide input voltage.

C. APWM Control Using PI Controller

Generally, FM, PSM, and APWM control schemes are employed in RCs. Compared with FM control, PSM and APWM control can achieve a wide voltage conversion ratio [25]. In the

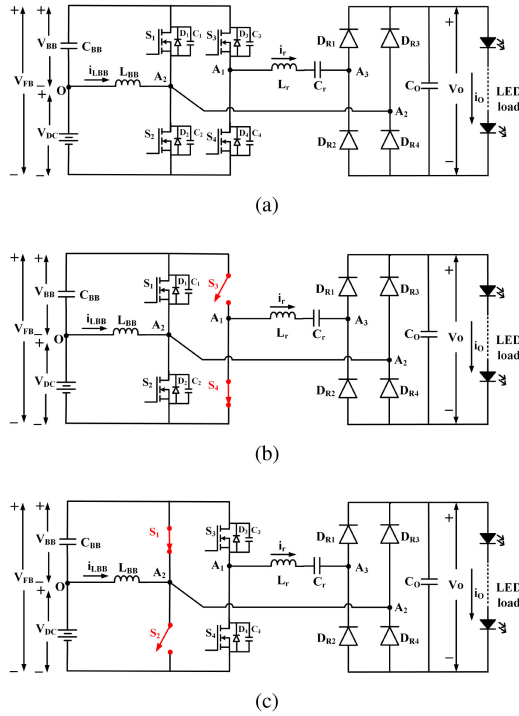


Fig. 2. Different reconfigurations of proposed LED driver under different input voltage ranges. (a) BB-FBSRC. (b) BB-HBSRC. (c) HBSRC.

proposed converter, PSM control can only be implemented in BB-FBSRC configuration as the remaining two configurations are HB-based topologies. However, by using only BB-FBSRC with phase shift control, ZVS can be achieved in all the switches for only smaller input voltage range. Hence, a simple APWM control is optimal and is employed in all the three configurations of the proposed converter for output voltage regulation. The schematic of the closed-loop control is shown in Fig. 1. Digital control is employed using digital signal processor (DSP). Three different PI controllers are employed for the three configurations. The input and output voltages are measured and fed to the DSP. The required illumination level is set in terms of dimming signal duty cycle D_{Dim} and corresponding low-frequency dimming signal is generated. Based on the input voltage range, the switches are configured to one of the three configurations and the corresponding PI output is enabled. The PI controller develops the required duty cycle (D) of high-frequency PWM signals based on the actual output voltage and reference voltage. These PWM signals and the dimming signal are combined using AND logic, producing the gate signals V_{g1} to V_{g4} for the switches S_1 to S_4 respectively.

D. Principle of Operation

The operations of BB-FBSRC and BB-HBSRC are similar and HBSRC is the conventional converter. Hence, the principle and modes of operation are discussed only for BB-FBSRC. The key waveforms of BB-FBSRC are shown in Fig. 3(a). The gate signals V_{g1} and V_{g2} are complementary to each other and the gate signals V_{g3} and V_{g4} are complementary to each other. V_{FB}

is the sum of two voltages, V_{dc} and V_{BB} , which is applied across the FB inverter. The FB inverter output voltage v_{A1-A2} results in i_r that flows through the LED load after rectification.

The operation of BB-FBSRC is divided into six modes and the equivalent circuit of each mode is shown in Fig. 3(b)–(g) and explained as follows.

1) *Mode-1* [t_1 – t_2]: The zero voltage across S_2 and S_3 due to the prior conduction of diodes D_2 and D_3 results in ZVS turn-ON when the gate signals are provided at $t = t_1$. The currents i_{LBB} and i_r continue to rise in the positive direction and their resultant flows in S_2 as shown in Fig. 3(b).

2) *Mode-2* [t_2 – t_3]: When S_2 and S_3 are turned OFF at $t = t_2$, C_2 and C_3 charge and C_1 and C_4 discharge respectively. Resonance condition takes place between the inductors and capacitors for a short duration. Assuming i_r and i_{LBB} to be constant during this short interval of operation, half of their resultant current flows through each capacitor as illustrated in Fig. 3(c).

3) *Mode-3* [t_3 – t_4]: At $t = t_3$, as C_1 and C_4 are completely discharged, D_1 and D_4 become forward biased. The inductor L_{BB} starts demagnetizing and, also, i_r starts decreasing. Thus, the current in the diodes starts raising from negative value. The diode D_1 current is the sum of i_{LBB} and i_r as illustrated in Fig. 3(d). The duration [t_2 – t_4] can be considered as dead time (t_d).

4) *Mode-4* [t_4 – t_5]: The conduction of D_1 and D_4 prior to this mode makes S_1 and S_4 ZVS turn-ON when the gate signals are provided at $t = t_4$. i_{LBB} and i_r continue to decrease and their resultant flows in S_1 as shown in Fig. 3(e).

5) *Mode-5* [t_5 – t_6]: At $t = t_5$, when S_1 and S_4 are turned OFF, C_2 and C_3 discharge and C_1 and C_4 charge, respectively. Resonance condition takes place between the inductors and capacitors for a short duration. Assuming i_r and i_{LBB} to be constant in this short duration, half of the resultant current shared by each capacitor as illustrated in Fig. 3(f).

6) *Mode-6* [t_6 – t_7]: At $t = t_6$, C_2 and C_3 are completely discharged and, hence, D_2 and D_3 start conducting. The current i_r starts raising. Also, due to magnetization, the current i_{LBB} increases linearly. Thus, the diode currents start increasing from negative value. The resultant current due to i_{LBB} and i_r flows in D_2 as illustrated in Fig. 3(g). The duration [t_5 – t_7] can be considered as dead time (t_d). This mode ends when gate signals are provided to switches S_2 and S_3 .

III. ANALYSIS OF PROPOSED CONVERTER

A. Voltage Gain

Analysis of BB-FBSRC is carried out under steady state with the assumption of ideal devices (MOSFETs and diodes) and constant output current. The voltage V_{BB} due to integrated BB operation is obtained as

$$V_{BB} = \frac{D}{(1-D)} V_{dc}. \quad (1)$$

The total input voltage V_{FB} applied to the BB-FBSRC is expressed as

$$V_{FB} = V_{dc} + V_{BB} = V_{dc} + \frac{D}{(1-D)} V_{dc} = \frac{V_{dc}}{(1-D)}. \quad (2)$$

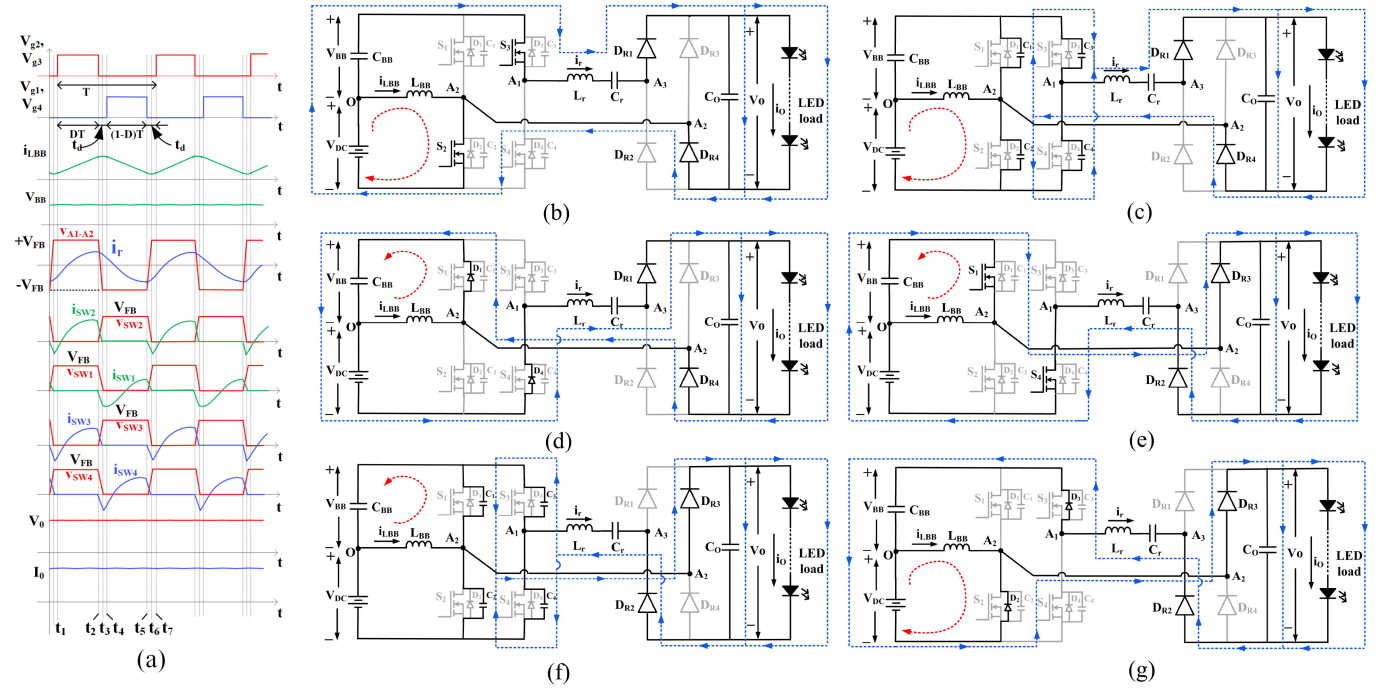


Fig. 3. BB-FBSRC key waveforms and operating modes. (a) Key waveforms. (b) Mode-1. (c) Mode-2. (d) Mode-3. (e) Mode-4. (f) Mode-5. (g) Mode-6.

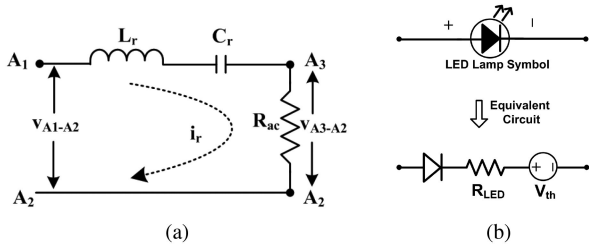


Fig. 4. (a) AC equivalent circuit. (b) LED symbol and equivalent circuit.

Square wave voltage with a magnitude of V_{FB} that is obtained from FB inverter is applied across $L_r - C_r$ network. As the fundamental components of the voltage and current of the resonant network is sinusoidal in nature, classical ac analysis can be carried out [31]. The ac equivalent circuit of the proposed configuration is shown in Fig. 4(a).

From Fig. 4(a), the voltage gain can be expressed as

$$\frac{V_{A3-A2}}{V_{A1-A2}} = \frac{R_{ac} \sin(\pi D)}{R_{ac} + j(X_{Lr} - X_{Cr})} \quad (3)$$

where

$$X_{Lr} = 2\pi f_s L_r; \quad X_{Cr} = \frac{1}{2\pi f_s C_r}; \quad R_{ac} = \frac{8}{\pi^2} R_O. \quad (4)$$

V_{A1-A2} and V_{A3-A2} are input and output voltages of the resonant network, respectively.

The voltage gain of BB-FBSRC can be expressed in terms of circuit parameters as

$$G_1 = \frac{V_O}{V_{dc}} = \frac{\sin(\pi D)}{(1-D) \left[1 + j \left(\frac{X_{Lr} - X_{Cr}}{R_{ac}} \right) \right]}. \quad (5)$$

Quality factor (Q) can be defined as

$$Q = \frac{\omega_r L_r}{R_{ac}} = \frac{1}{\omega_r C_r R_{ac}}. \quad (6)$$

The angular resonant frequency ω_r is given by

$$\omega_r = 2\pi f_r = \frac{1}{\sqrt{L_r C_r}} \quad (7)$$

where f_r is the resonant frequency in Hz. By substituting (4) and (6) into (5), the gain of BB-FBSRC is obtained as

$$G_1 = \frac{V_O}{V_{dc}} = \frac{\sin(\pi D)}{(1-D) \left[1 + j \frac{\pi^2}{8} Q \left(\frac{f_s}{f_r} - \frac{f_r}{f_s} \right) \right]}. \quad (8)$$

Similarly the gain of BB-HBSRC is obtained as

$$G_2 = \frac{V_O}{V_{dc}} = \frac{\sin(\pi D)}{2(1-D) \left[1 + j \frac{\pi^2}{8} Q \left(\frac{f_s}{f_r} - \frac{f_r}{f_s} \right) \right]} \quad (9)$$

and the gain of HBSRC is obtained as

$$G_3 = \frac{V_O}{V_{dc}} = \frac{\sin(\pi D)}{2 \left[1 + j \frac{\pi^2}{8} Q \left(\frac{f_s}{f_r} - \frac{f_r}{f_s} \right) \right]}. \quad (10)$$

B. Switch Currents and Critical Inductance L_{BB}

Analysis of soft switching operation and device peak current stress is based on the instantaneous values of switch currents. The current in resonant inductor i_r at any instant for BB-FBSRC can be given as

$$i_{r1}(t) = \frac{4V_{dc}\sin(\pi D)\sin(\omega_s t + \alpha - \phi)}{(1-D)\pi Z_{in}} \quad (11)$$

where

$$\left. \begin{aligned} \phi &= \tan^{-1} \left(\frac{X_{Lr} - X_{Cr}}{R_{ac}} \right) \\ \alpha &= \tan^{-1} \left(\frac{\sin(2\pi D)}{1 - \cos(2\pi D)} \right) \\ Z_{in} &= R_{ac} + j(X_{Lr} - X_{Cr}) \end{aligned} \right\}. \quad (12)$$

Similarly, the current i_r at any instant for BB-HBSRC can be given as

$$i_{r2}(t) = \frac{2V_{dc}\sin(\pi D)\sin(\omega_s t + \alpha - \phi)}{(1-D)\pi Z_{in}} \quad (13)$$

and the current i_r at any instant for HBSRC can be given as

$$i_{r3}(t) = \frac{2V_{dc}\sin(\pi D)\sin(\omega_s t + \alpha - \phi)}{\pi Z_{in}}. \quad (14)$$

The average source current can be expressed in terms of average inductor current as [27]

$$I_{dc} \approx (I_{LBB} + I_r) \approx I_{LBB} \quad (15)$$

For 100% efficiency

$$V_{dc}I_{dc} = V_o I_o = P_o.$$

Hence,

$$I_{dc} = \frac{P_o}{V_{dc}}. \quad (16)$$

The minimum and maximum currents in L_{BB} are expressed as

$$I_{LBBmin} = I_{LBB} - \frac{\Delta i_{LBB}}{2} \quad (17)$$

$$I_{LBBmax} = I_{LBB} + \frac{\Delta i_{LBB}}{2} \quad (18)$$

where the inductor ripple $\Delta i_{LBB} = (I_{LBBmax} - I_{LBBmin})$ is expressed as

$$\Delta i_{LBB} = \frac{V_{dc}DT}{L_{BB}}. \quad (19)$$

Thus, by substituting (15), (16), and (19) in (17) and making $I_{LBBmin} = 0$, the critical inductance of BB inductor L_{BBcr} is expressed as

$$L_{BBcr} = \frac{V_{dc}^2 D}{2P_o f_s} \quad (20)$$

where f_s is the switching frequency.

For continuous conduction, $L_{BB} > L_{BBcr}$.

The instantaneous current of L_{BB} can be expressed as

$$i_{LBB}(t) = \begin{cases} \frac{\Delta i_{LBB}}{DT}t + I_{LBBmin}, & 0 \leq t < DT \\ \frac{\Delta i_{LBB}}{(D-1)T}(t-DT) + I_{LBBmax}, & DT \leq t < T. \end{cases} \quad (21)$$

From Fig. 3(a), the instantaneous currents in the switches can be expressed as follows.

$i_{S1}(t)$ in BB-FBSRC and BB-HBSRC operation is

$$i_{S1}(t) = \begin{cases} 0, & 0 \leq t < DT \\ -(i_r(t) + i_{LBB}(t)), & DT \leq t < T. \end{cases} \quad (22)$$

$i_{S1}(t)$ in HBSRC operation is

$$i_{S1}(t) = -i_r(t). \quad (23)$$

$i_{S2}(t)$ in BB-FBSRC and BB-HBSRC operation is

$$i_{S2}(t) = \begin{cases} (i_{LBB}(t) + i_r(t)), & 0 \leq t < DT \\ 0, & DT \leq t < T. \end{cases} \quad (24)$$

$i_{S2}(t) = 0$ in HBSRC operation. $i_{S3}(t)$ in BB-FBSRC and HBSRC operation is

$$i_{S3}(t) = \begin{cases} i_r(t), & 0 \leq t < DT \\ 0, & DT < t \leq T. \end{cases} \quad (25)$$

$i_{S3}(t) = 0$ in BB-HBSRC operation. $i_{S4}(t)$ in BB-FBSRC and HBSRC operation is

$$i_{S4}(t) = \begin{cases} 0, & 0 \leq t < DT \\ -i_r(t), & DT \leq t < T. \end{cases} \quad (26)$$

$i_{S4}(t)$ in BB-HBSRC operation is

$$i_{S4}(t) = -i_r(t). \quad (27)$$

C. ZVS Condition

Due to the BB integration, along with resonant current i_r , the inductor current i_{LBB} also flows in the switches S_1 and S_2 . As both the currents are positive, the turn-ON current of switch S_1 from (22) at $t = t_2 \approx DT$ is more negative. Thus, ZVS turn-ON can be inherently achieved by it. But, due to the difference of currents, i.e., positive current of i_{LBB} and negative current of i_r , the turn-ON current of switch S_2 from (24) at $t = t_5 \approx T$ is affected. Thus, for achieving ZVS turn-ON across the switches S_1 and S_2 , the ZVS criteria is considered with switch S_2 at $t = t_5 \approx T$ and is expressed as

$$C_{oss}V_{FB}^2 < \frac{1}{2}L_{BB}i_{LBB}^2(t_5) - \frac{1}{2}L_r i_r^2(t_5) \quad (28)$$

where C_{oss} is the output capacitance of MOSFET switches.

The condition of ZVS in (28) must be satisfied for all the voltage ranges in order to achieve ZVS turn-ON across S_1 and S_2 devices.

The switches S_3 and S_4 are independent of BB operation. However, due to PWM control, ZVS turn-ON is affected for the switch operating for duration $< (T/2)$. For $D < 0.5$, ZVS turn-ON of switch S_3 is affected and for $D > 0.5$, ZVS turn-ON of switch

S_4 is affected. Thus, the ZVS criteria for $D < 0.5$ is considered with switch S_3 at $t = t_2 \approx DT$ in Fig. 3(a) and is expressed based on (25) as

$$C_{oss} V_{FB}^2 < \frac{1}{2} L_r i_r^2(t_2). \quad (29)$$

Similarly, the ZVS criteria for $D > 0.5$ is considered with switch S_4 at $t = t_5 \approx T$ in Fig. 3(a) and is expressed as based on (26)

$$C_{oss} V_{FB}^2 < \frac{1}{2} L_r i_r^2(t_5). \quad (30)$$

If one of the above two equations that are having lower duty cycle among all the three configurations is satisfied, then S_3 and S_4 have ZVS turn-ON for all other configurations with different input voltages. Thus, if (28), (29), and (30) are satisfied, ZVS can be achieved across all the switches.

D. Conduction Losses

In the proposed converter, the rectifier diodes are soft switched and ZVS turn-ON is achieved in the switches due to the series resonance. The switch turn-OFF losses are less. Hence, the main losses in the proposed converter are conduction losses in the switches and diodes. These conduction losses play a vital role in estimating the efficiency of the converter. The current expressions for estimating the conduction losses are expressed as below. The peak current of i_r in BB-FBSRC is given by

$$I_{r1_max} = \frac{4V_{dc} \sin(\pi D)}{(1-D)\pi Z_{in}} \quad (31)$$

Similarly for BB-HBSRC

$$I_{r2_max} = \frac{2V_{dc} \sin(\pi D)}{(1-D)\pi Z_{in}} \quad (32)$$

and for HBSRC

$$I_{r3_max} = \frac{2V_{dc} \sin(\pi D)}{\pi Z_{in}}. \quad (33)$$

The inductor current i_{LBB} flowing in BB-FBSRC and BB-HBSRC can be split into ac rms and dc currents and expressed as follows:

$$I_{LBB_dc} = I_{LBB} = \frac{P_O}{V_{dc}}; \quad I_{LBB_ac} = \Delta i_{LBB} \sqrt{\frac{1}{12}}. \quad (34)$$

In BB-FBSRC, the currents i_r and i_{LBB} flows in S_2 for a duration of DT and then flows in S_1 for the remaining duration. Similarly, the current i_r flows in S_4 for a duration of DT and then flows in S_3 for the remaining duration. Thus, the total conduction losses of the four switching devices can be given as [32]

$$P_{1_cond_Switches} = (I_{r1_max}^2 + I_{LBB_dc}^2 + I_{LBB_ac}^2) r_{DS} \quad (35)$$

where r_{DS} is the MOSFET drain to source ON-resistance.

In BB-HBSRC, the currents i_r and i_{LBB} flow in S_2 for a duration of DT and then flows in S_1 for the remaining duration. Further, S_3 is continuously OFF and S_4 is continuously ON carrying the current of i_r in it. Thus, the total conduction losses of the three switching devices can be given as

$$P_{2_cond_Switches} = (I_{r2_max}^2 + I_{LBB_dc}^2 + I_{LBB_ac}^2) r_{DS}. \quad (36)$$

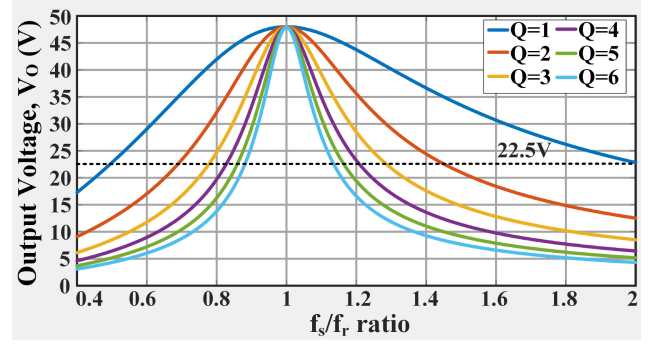


Fig. 5. LC resonance characteristics.

In HBSRC, S_1 is continuously ON carrying the current of i_r in it and S_2 is continuously OFF. Also, the current i_r flows in S_4 for a duration of DT and then flows in S_3 for the remaining duration. Thus, the total conduction losses of the three switching devices can be given as

$$P_{3_cond_Switches} = (I_{r3_max}^2) r_{DS}. \quad (37)$$

The rectifier diode conduction losses in all the three configurations can be expressed as

$$P_{cond_Diodes} = 2V_f I_o + \frac{\pi^2 I_o^2 R_f}{4} \quad (38)$$

where V_f and R_f are the diode forward offset voltage and diode forward resistance, respectively.

IV. DESIGN CONSIDERATIONS

A. Design Parameters for LED Lamp

The LED lamp symbol and its equivalent circuit are shown in Fig. 4(b) where V_{th} is its threshold voltage and R_{LED} is the LED resistance. The LEDs used for experimentation are TMX HP3W white LEDs. Each LED considered is having a V_{th} of 2.321 V. Two strings of seven LEDs each are considered to design a load of 22.77 W/22.505 V that results in a V_{th} of 16.247 V and a current of 1.012 A.

B. Resonant Elements and D Limits of HBSRC

The input voltage and resonant elements are selected based on HBSRC configuration, as this topology is simple without BB operation integrated. In order to operate an LED load with voltage V_o of 22.5 V in all the three configurations, the input voltage V_{dc} is selected as 96 V with the converter operating as HBSRC at $D = 50\%$. The design of resonant elements is similar to conventional procedure. From (10), the output voltage versus nominal frequency ($\frac{f_s}{f_r}$) has been plotted at $D = 50\%$ with different Q values as shown in Fig. 5. To obtain the required V_o of 22.5 V with V_{dc} of 96 V, from the graph, the Q -factor, frequency ratio ($\frac{f_s}{f_r}$) are selected as 4.14 and 1.2, respectively. With f_s of 200 kHz and the ratio f_s/f_r as 1.2, L_r is obtained as 88 μH from (4) and (6). From (7), the L_r and C_r product can

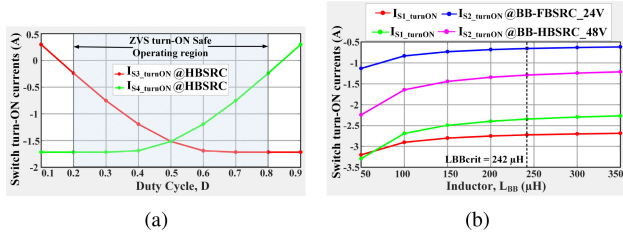


Fig. 6. ZVS condition of switches (a) S_3 and S_4 under duty cycle variation in HBSRC and (b) S_1 and S_2 with different L_{BB} values in BB-FBSRC and BB-HBSRC at $D = 50\%$.

be expressed as

$$L_r C_r = 0.91344 \times 10^{-12}. \quad (39)$$

From (39), C_r is obtained as 10.31 nF . The turn-ON currents of switches S_3 and S_4 are estimated from the instantaneous current equations (25) and (26) at $t \approx DT$ and $t \approx T$, respectively. Fig. 6(a) shows the variation of switch turn-ON currents of S_3 and S_4 with duty cycle variation. As can be observed, ZVS turn-ON is affected for the switch operating for duration $<(T/2)$. As the switch currents are symmetrical to each other, for $D < 0.5$, ZVS turn-ON of switch S_3 is affected and for $D > 0.5$, ZVS turn-ON of switch S_4 is affected. The safe duty cycle operating region for ZVS turn-ON for the switches S_3 and S_4 is $0.2 < D < 0.8$ as shown in Fig. 6(a) with HBSRC and is true even for BB-FBSRC and BB-HBSRC. Thus, the HBSRC is operated from 96 V at $D = 0.5$ to 120 V at $D = 0.3$.

C. Computing L_{BB} and D Limits of BB-FBSRC and BB-HBSRC

The input voltage V_{dc} of BB-FBSRC and BB-HBSRC at $D = 50\%$ are computed from (8) and (9), respectively, with same resonant circuit parameters to produce V_o of 22.5 V.

In BB-FBSRC and BB-HBSRC configurations, the ZVS operation of switches S_1 and S_2 is affected as these devices are integrated with BB operation. Fig. 6(b) shows the turn-ON currents of switches S_1 and S_2 for different values of L_{BB} under BB-FBSRC and BB-HBSRC operation with $V_{dc} = 24$ and 48 V, respectively, at $D = 0.5$. The turn-ON currents of switches S_1 and S_2 are estimated from the instantaneous current equations (22) and (24) at $t \approx DT$ and $t \approx T$, respectively. It can be observed from Fig. 6(b) that the switch S_2 is having less negative current compared to S_1 , and, hence, ZVS turn-ON in S_2 ensures the same in S_1 . Also, it can be observed that as L_{BB} increases beyond L_{BBcr} , the turn-ON currents remain almost constant. But, as L_{BB} decreases less than L_{BBcr} , the switch currents decrease and become more negative. Hence, ZVS turn-ON capability increases. The absolute values of peak currents in the switches S_1 and S_2 are estimated from (22) and (24) in the range of $0 \leq t < T$ and using which the corresponding conduction losses are estimated from (35), (36), and (38). Fig. 7 shows the peak currents of S_1 and S_2 and the total conduction losses of the converter for different values of L_{BB} under BB-FBSRC and BB-HBSRC operation with $V_{dc} = 24$ and

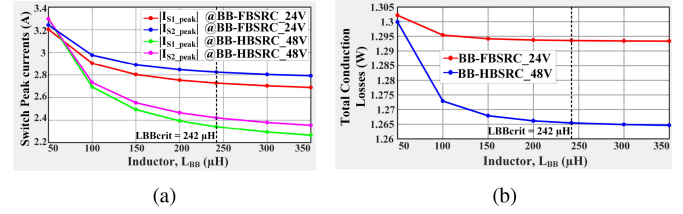


Fig. 7. With different values of L_{BB} . (a) Switch peak currents. (b) Total conduction losses.

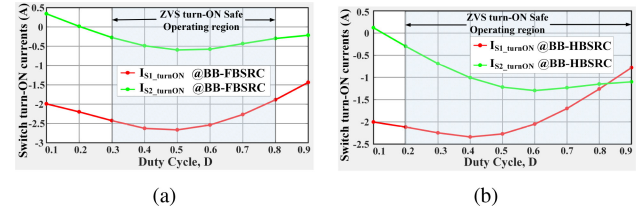


Fig. 8. ZVS condition with duty cycle variation across switches (a) S_1 and S_2 in BB-FBSRC and (b) S_1 and S_2 in BB-HBSRC.

48 V, respectively, at $D = 0.5$. It can be observed that even though ZVS capability increases with $L_{BB} < L_{BBcr}$, the switch peak currents and, hence, the conduction losses are increasing. Beyond L_{BBcr} , the switch peak currents and conduction losses are almost constant. This is true even with other input voltages. Thus, to have better efficiency, L_{BB} is chosen as $262 \mu\text{H}$ which is little more than L_{BBcr} . However, even a lesser value of L_{BB} can be chosen if the converter is to be compact in size as there is no much deviation in the losses. Fig. 8 shows the turn-ON currents in switches S_1 and S_2 with BB-FBSRC and BB-HBSRC operation at different duty cycles with $L_{BB} = 262 \mu\text{H}$. It can be observed from Fig. 8(a), the safe range of duty cycle for ZVS turn-ON for BB-FBSRC is $0.3 < D < 0.8$. Similarly, from Fig. 8(b), this range is obtained for BB-HBSRC as $0.2 < D < 0.9$. Hence, the range of input voltage for BB-FBSRC is selected as 18–36 V with $D = 0.68$ –0.34. The range of input voltage for BB-HBSRC is selected as 36–96 V with $D = 0.68$ to 0.26. Fig. 9(a) shows the input voltage V_{dc} versus duty cycle D variation for all the three configurations. Hence, the selected duty cycle limits results in better control of the input voltages and provide ZVS turn-ON of the switches in all the three configurations. Fig. 9(b) shows the duty cycle versus gain variation, in which it can be observed that there is a wide variation in the voltage gain and even it is above and below unity, producing buck/boost modes. Thus, the converter is operated optimally.

D. Selection of MOSFET Switches

The drain–source peak voltage of the switches is the voltage V_{FB} applied to the inverter. Fig. 10(a) shows the switch drain–source peak voltages in the entire input voltage range under different configurations. The peak voltages are equal for all the switches at particular input voltage level and zero for the switch which is continuously ON. In BB-FBSRC, the switches (S_1 – S_4) have a maximum drain to source voltage of

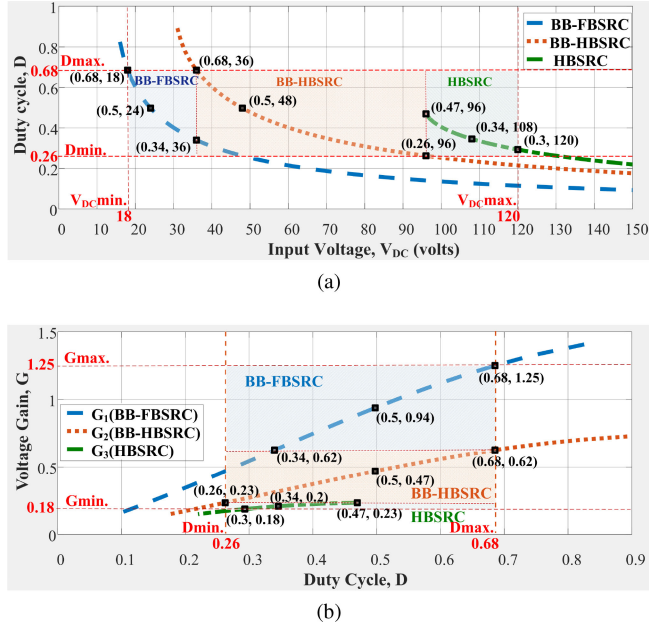


Fig. 9. (a) Variation of duty cycle with respect to input voltage variation. (b) Variation of voltage gain with respect to duty cycle variation.

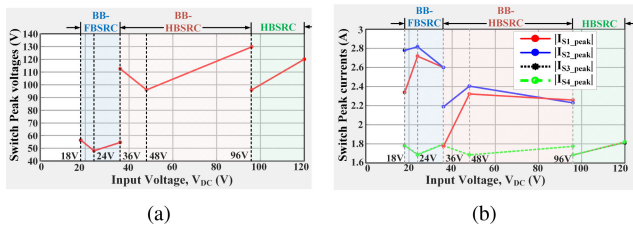


Fig. 10. In all the voltage ranges: (a) variation of switch drain–source peak voltages; and (b) variation of switch drain–source peak currents.

$V_{FB} = 56.25$ V at $V_{dc} = 18$ V and $D = 0.68$. Similarly, in BB-HBSRC, the switches (S_1 , S_2 , and S_4) have a maximum drain to source voltage of $V_{FB} = 131$ V at $V_{dc} = 96$ V and $D = 0.26$. However, in HBSRC, the drain to source voltage applied is only $V_{FB} = V_{dc}$ as $V_{BB} \approx 0$. Thus, in HBSRC, the maximum voltage across the switches (S_2 , S_3 , and S_4) is the maximum input voltage V_{dc} , i.e., 120 V. Hence, the switches S_1 , S_2 , and S_3 have maximum peak voltage stress of 131 V and the switch S_4 has maximum peak voltage stress of 120 V. Hence, the peak voltage stress across switches is not high and is on par with the input voltage applied. The absolute values of peak currents in the switches S_1 and S_4 are estimated from (22)–(27) in the range of $0 \leq t < T$. Fig. 10(b) shows the absolute values of switch peak drain currents in the entire input voltage range under different configurations. It can be observed that the switch peak currents are more in BB-FBSRC configuration due to the increased BB average current I_{LBB} with less input voltage. The maximum peak currents in the switches are in the range of 1.8–2.8 A. Thus, it can be observed from figure that the variation in peak currents in switches S_3 and S_4 is very less in each configuration and they are almost of the same magnitude in all the configurations. As

TABLE I
DESIGN PARAMETERS

Parameters	Values
DC Input voltage, V_{DC}	18–120 V
Switching frequency, f_s	200 kHz
Resonant frequency, f_r	166.53 kHz
Resonant inductor, L_r	88 μ H
Resonant capacitor, C_r	10 nF
Output capacitor, C_o	5 μ F
Output voltage, V_o	22.505V
Output current, I_o	1.012 A
Output power, P_o	22.77 W
Buck-boost inductor, L_{BB}	260 μ H
Buck-boost capacitor, C_{BB}	15 μ F
PWM dimming frequency	200 Hz
MOSFETs	IRFP250N
Diodes	MBR2000CT

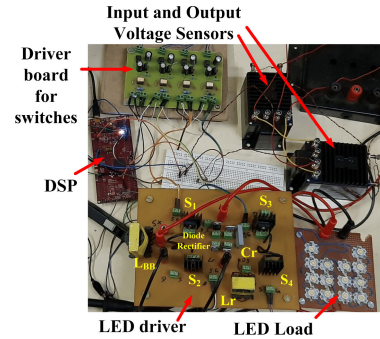


Fig. 11. Experimental setup of the proposed LED driver.

BB current also flows in switches S_1 and S_2 , the peak currents increase a bit, compared with currents in S_3 and S_4 ; however, they are not of high value. Thus, the peak current stress in the switches is not high and it is at a reasonable value. Based on the peak voltages and currents, the MOSFET switches IRFP250NPbF are selected in the proposed configuration having r_{DS} of 75 $m\Omega$.

V. SIMULATION AND EXPERIMENTAL RESULTS

The proposed configuration is simulated and tested for the input voltage range of 18–120 V. The corresponding operating voltage range and duty cycle of particular configuration are considered as in Fig. 9(a) with the parameters shown in Table I. Fig. 11 shows the experimental setup of the proposed LED driver. CV 3-200/SP6 and CV 3-500 voltage sensors are used for input and output voltage sensing. DSP-TMS320F28379D is used for generating the gate signals using closed-loop control. The proposed converter closed-loop behavior is simulated in PSim Software. Fig. 12 shows the simulated dynamic behavior of the proposed configuration with V_{dc} varying from 18 to 120 V, where the proposed configuration shows that it can well reconfigure in different configurations based on the input voltage range and well regulated within particular reconfiguration. Fig. 13 shows the experimental dynamic behavior of the proposed configuration while transforming from one configuration to another based on the input voltage. Fig. 14 shows the experimental dynamic behavior of the proposed converter in each configuration. As can be observed, there is significantly

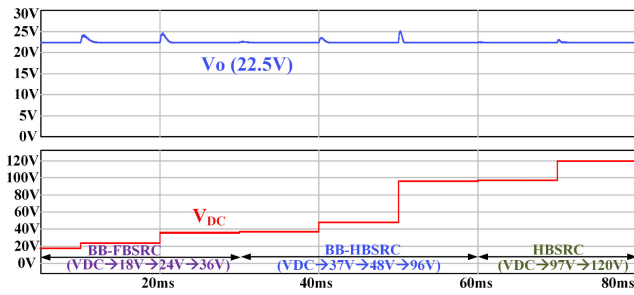


Fig. 12. Simulated dynamic behavior of proposed configuration with $V_{dc} = 18\text{--}120\text{ V}$.

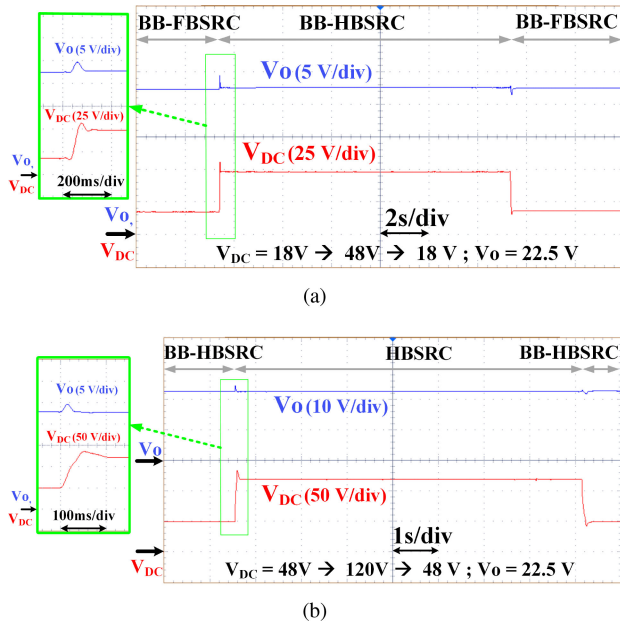


Fig. 13. Experimental dynamic behavior of proposed configuration under different reconfigurations with: (a) $V_{dc} = 18\text{--}48\text{--}18\text{ V}$ (BB-FBSRC to BB-HBSRC to BB-FBSRC); (b) $V_{dc} = 48\text{--}120\text{--}48\text{ V}$ (BB-HBSRC to HBSRC to BB-HBSRC).

less overshoot and faster response compared with simulation results, which indicates that the proposed converter is stable even under dynamic conditions. Thus, the proposed converter can smoothly transform from one configuration to another and can well regulate the output voltage in each configuration, and it, thus, regulates the output voltage for the wide input voltage variation from 18 to 120 V. To know the exact behavior of the proposed converter in steady state, it is simulated in PSpice software. Figs. 15–23 show the simulation and experimental waveforms of proposed converter in steady state. The simulation and experimental results of BB-FBSRC with $V_{dc} = 24, 18,$ and 36 V and corresponding duty cycle as 50%, 68%, and 34%, respectively, are shown in Figs. 15–18. Fig. 15 shows the waveforms of $v_{BB}, i_{LBB}, v_{A1\text{--}A2},$ and i_r at various input voltages. Figs. 16–18 show the waveforms of drain to source voltages, $v_{S1\text{--}S4}$ and drain currents $i_{S1\text{--}S4}$ of switches $S_1\text{--}S_4$ at various input voltages. The ZVS turn-ON across the devices is observed and zero current switching (ZCS) turn-OFF is partially achieved

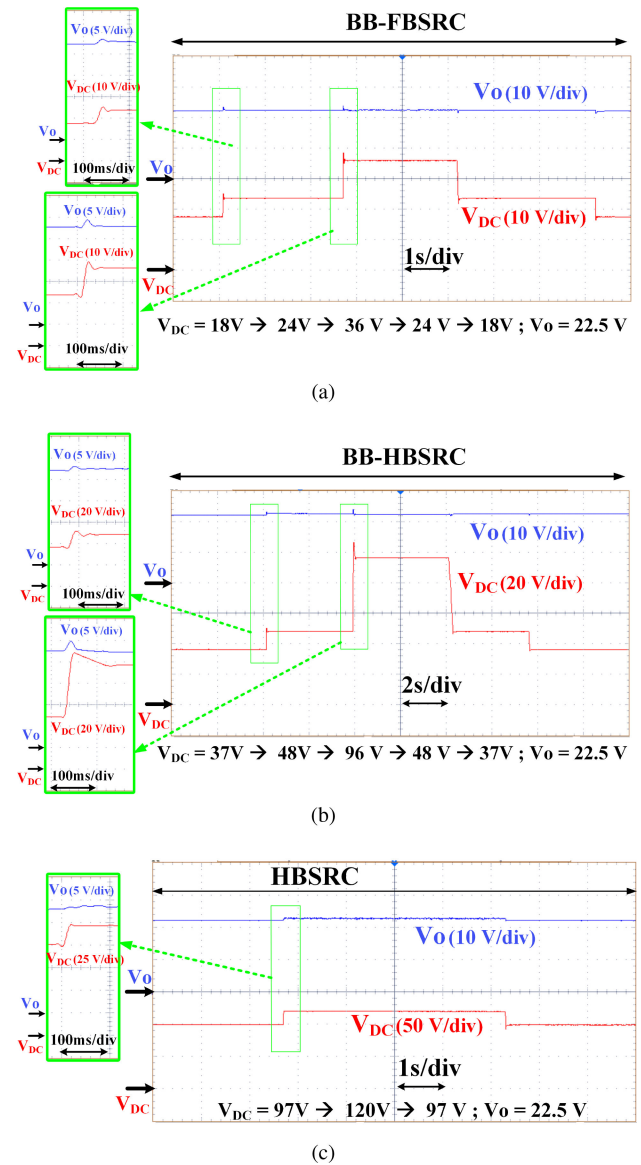


Fig. 14. Experimental dynamic behavior of proposed configuration in: (a) BB-FBSRC with $V_{dc} = 18\text{--}24\text{--}36\text{--}24\text{--}18\text{ V}$; (b) BB-HBSRC with $V_{dc} = 37\text{--}48\text{--}96\text{--}48\text{--}37\text{ V}$; (c) HBSRC with $V_{dc} = 97\text{--}120\text{--}97\text{ V}$.

for the above voltages; thus, soft-switching is achieved by the BB-FBSRC for the voltage range of 18–36 V. The simulation and experimental results of BB-HBSRC with $V_{dc} = 48, 36,$ and 96 V and corresponding duty cycle as 50%, 68%, and 26%, respectively, are shown in Figs. 19–21. As ZVS turn-OFF across the devices is observed and ZCS turn-ON is partially achieved for the above voltages, soft-switching is achieved by the BB-HBSRC for the voltage range of 36–96 V. The simulation and experimental results of HBSRC with $V_{dc} = 96$ and 120 V corresponding duty cycle as 50% and 30%, respectively, are shown in Figs. 22 and 23. As ZVS turn-OFF across the devices is observed and ZCS turn-ON is partially achieved for the above voltages, soft-switching is achieved by the HBSRC for the voltage range of 96–120 V. As discussed in Section III-C, the peak currents of S_1 and S_2 are varying in BB-FBSRC and BB-HBSRC as

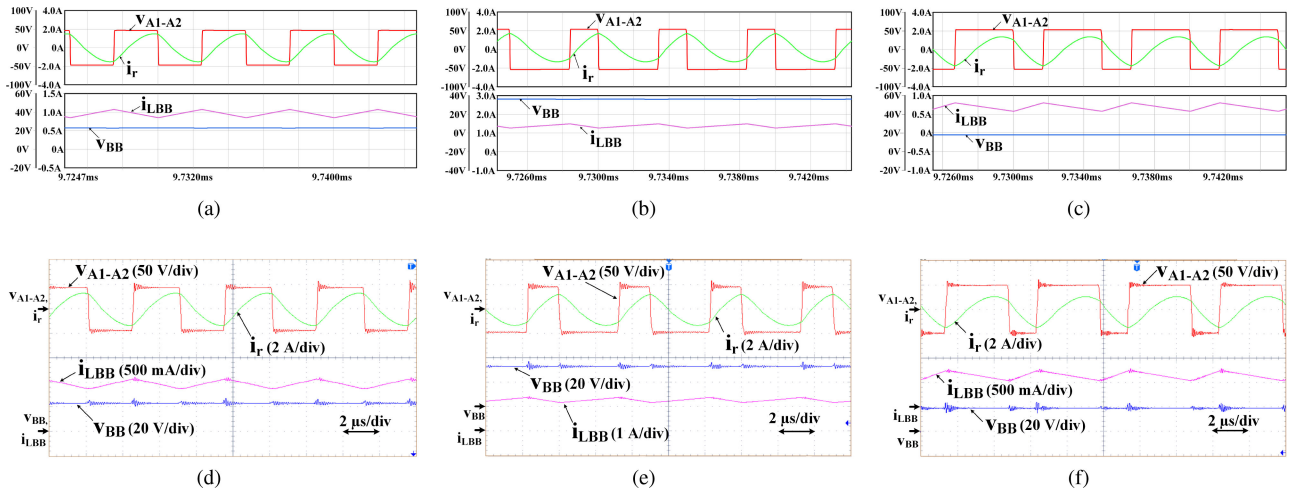


Fig. 15. Waveforms of v_{A1-A2} , i_r , v_{BB} , and i_{LBB} in BB-FBSRC at V_{dc} . (a) 24 V through simulation. (b) 18 V through simulation. (c) 36 V through simulation. (d) 24 V through experimentation. (e) 18 V through experimentation. (f) 36 V through experimentation.

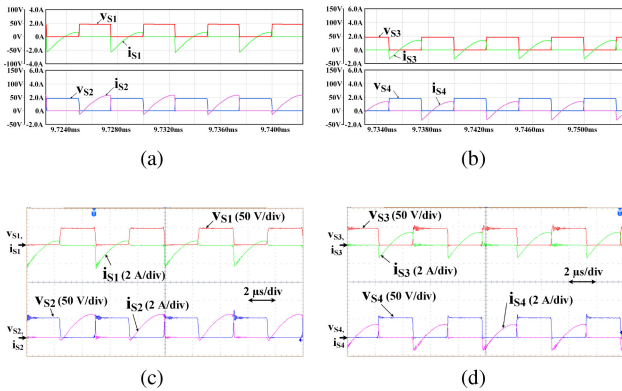


Fig. 16. Voltage and current waveforms of switches in BB-FBSRC at V_{dc} of 24 V through: (a) S_1, S_2 through simulation; (b) S_3, S_4 through simulation; (c) S_1, S_2 through experimentation; (d) S_3, S_4 through experimentation.

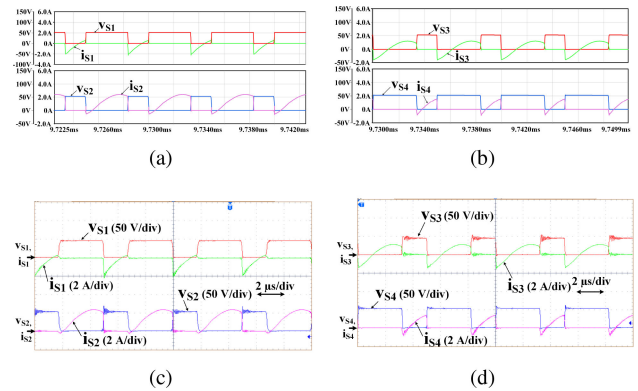


Fig. 17. Voltage and current waveforms of switches in BB-FBSRC at V_{dc} of 18 V through: (a) S_1, S_2 through simulation; (b) S_3, S_4 through simulation; (c) S_1, S_2 through experimentation; (d) S_3, S_4 through experimentation.

they have to carry i_{LBB} along with i_r and the switch S_2 is more sensitive to ZVS turn-ON. Also, as discussed, the switches S_4 for $D > 50\%$ and S_3 for $D < 50\%$ are sensitive to ZVS turn-ON in BB-FBSRC and HBSRC configuration. However, irrespective of inductor current and duty cycle modulation, the proposed converter achieves ZVS turn-ON across all the switches. Further, the simulation and experimental results are in good agreement.

In the proposed LED driver, dimming is implemented using PWM technique to regulate the illumination of the LED lamp, where the inverter is turned ON and OFF with a low dimming frequency. Thus, without disturbing the operating point of the LED lamp, its average current is regulated. The dimming operation is achieved in all the three configurations with a frequency of 200 Hz. Fig. 24 shows the experimental results of LED voltage and current at 40% and 80% dimming levels for BB-FBSRC, BB-HBSRC, and HBSRC at $V_{dc} = 24, 48, \text{ and } 96$ V, respectively. Similarly, dimming control can be implemented when the converter operated for other input voltage ranges.

VI. EFFICIENCY AND COMPARATIVE STUDY

The total conduction losses of the switches and diodes are estimated using (35)–(38) and efficiency curve for the entire input voltage range of 18–120 V has been plotted as shown in Fig. 26(a). Further, loss analysis using thermal modeling has been carried out in PSim Software. Fig. 25 shows the simulated loss analysis across switches for the entire input voltage range. The total diode losses obtained through simulation is same in entire voltage range and is 1.33 W. Corresponding efficiency curve is shown in Fig. 26(a). As the turn-OFF switching losses are also accounted in simulation, the simulated efficiency is low compared with theoretical efficiency. Fig. 26(a) also shows the practical measured efficiency. As there are core and winding losses also in practice, the experimental efficiency is little less compared to simulation efficiency. The efficiency is around 92%–94%. Thus, the proposed converter achieves high efficiency in all the configurations. Fig. 26(b) shows the efficiency curve of all the three configurations with 50% duty cycle at

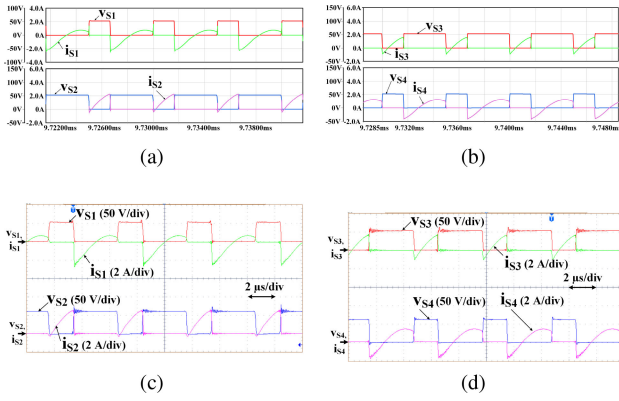


Fig. 18. Voltage and current waveforms of switches in BB-FBSRC at V_{dc} of 36 V through: (a) S_1, S_2 through simulation; (b) S_3, S_4 through simulation; (c) S_1, S_2 through experimentation; (d) S_3, S_4 through experimentation.

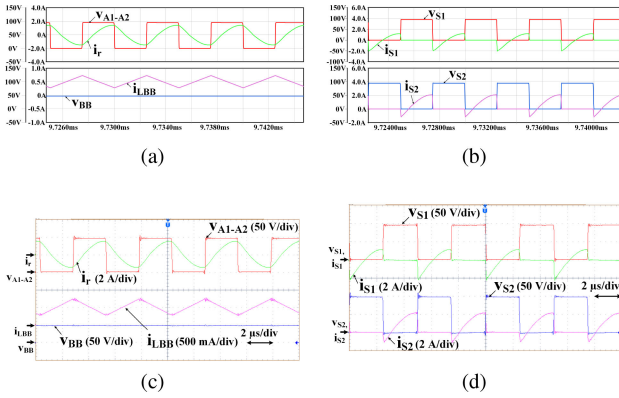


Fig. 19. Waveforms of voltages and currents in BB-HBSRC at $V_{dc} = 48$ V: (a) $v_{A1-A2}, i_r, v_{BB}, i_{LBB}$ through simulation; (b) S_1, S_2 through simulation; (c) $v_{A1-A2}, i_r, v_{BB}, i_{LBB}$ through experimentation; (d) S_1, S_2 through experimentation.

TABLE II
COMPARISON OF WIDE INPUT LED DRIVERS

Topologies	JSSC 2015 [6]	LM3405 2016 [7]	TIE 2017 [5]	TCAS1 2018 [9]	TPE 2019 [10]	Proposed
Process	0.35 μ m CMOS	N.A.	NA	0.5 μ m CMOS	0.13 μ m BCDLite	NA
Input Voltage (V)	5-45	3-15	7-45	5-115	6-18	18-120
Switching Mode	Hard-Switching	Hard-Switching	Hard-Switching	Auto Configurable Hard/Soft Switching	Soft-Switching	Soft-Switching
Average LED current (mA)	700	1000	1000	350	500-1300	1000
Max. Output Power (W)	26	15	25	25	12	22.77
Switching Frequency	4MHz	1.6MHz	500kHz	2.2MHz and 1.6MHz	2.8MHz	200 kHz
Inductor (μ H)	8.2-39	6.8 & 22	10	10	0.68-1	88 & 260
Dimming Frequency	20kHz	20kHz	1kHz	20kHz	20kHz	200 Hz
Max. Power Efficiency	97.2	91	82-96	92.6 and 94.4	96.1	91.8-94.19

different dimming levels. It can be noticed that the efficiency is nearly constant in all the three configurations.

The proposed configuration is compared with existing LED drivers that operate for wide input applications as shown in Table II. The component count is less in these topologies. But

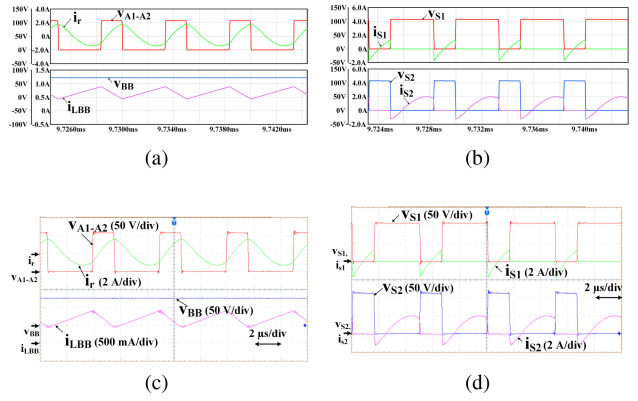


Fig. 20. Waveforms of voltages and currents in BB-HBSRC at $V_{dc} = 36$ V: (a) $v_{A1-A2}, i_r, v_{BB}, i_{LBB}$ through simulation; (b) S_1, S_2 through simulation; (c) $v_{A1-A2}, i_r, v_{BB}, i_{LBB}$ through experimentation; (d) S_1, S_2 through experimentation.

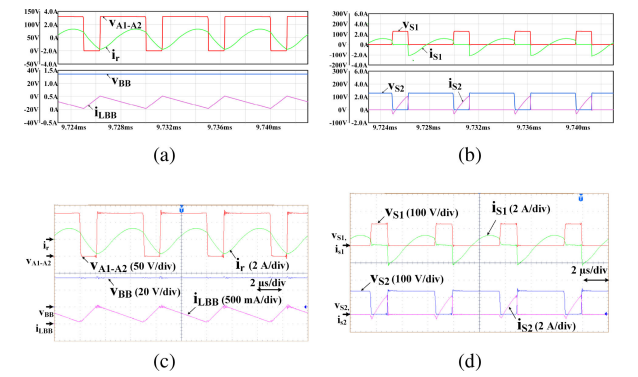


Fig. 21. Waveforms of voltages and currents in BB-HBSRC at $V_{dc} = 96$ V: (a) $v_{A1-A2}, i_r, v_{BB}, i_{LBB}$ through simulation; (b) S_1, S_2 through simulation; (c) $v_{A1-A2}, i_r, v_{BB}, i_{LBB}$ through experimentation; (d) S_1, S_2 through experimentation.

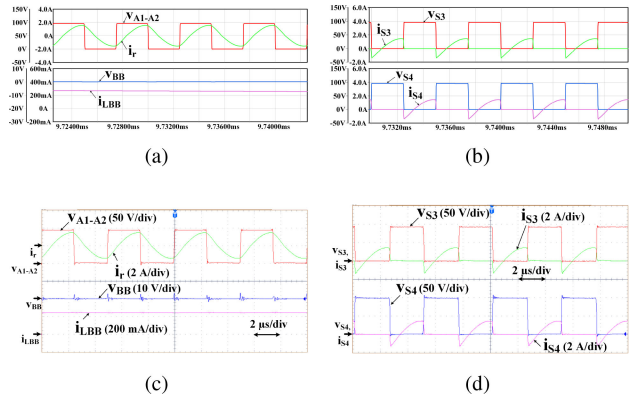


Fig. 22. Waveforms of voltages and currents in HBSRC at $V_{dc} = 96$ V: (a) $v_{A1-A2}, i_r, v_{BB}, i_{LBB}$ through simulation; (b) S_3, S_4 through simulation; (c) $v_{A1-A2}, i_r, v_{BB}, i_{LBB}$ through experimentation; (d) S_3, S_4 through experimentation.

in [5]–[7], the converters are operated with hard-switching that either reduces the power density or increases the switching losses. Also, in [6], [9], and [10], CMOS and BCDLite technologies are implemented which increase the cost and complexity. Thus, compared with existing LED drivers

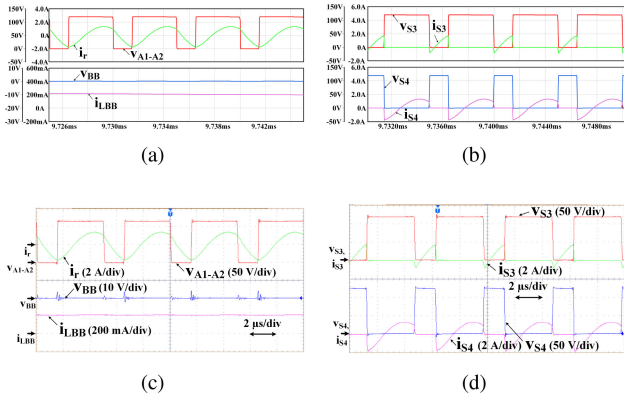


Fig. 23. Waveforms of voltages and currents in HBSRC at $V = 120$ V: (a) v_{A1-A2} , i_r , v_{BB} , i_{LBB} through simulation; (b) S_3 , S_4 through simulation; (c) v_{A1-A2} , i_r , v_{BB} , i_{LBB} through experimentation; (d) S_3 , S_4 through experimentation.

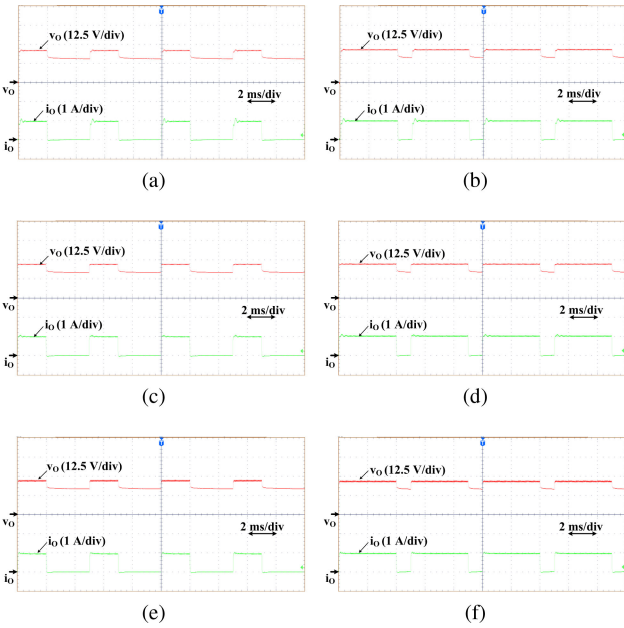


Fig. 24. Experimental dimming waveforms of v_o , i_o . (a) BB-FBSRC with 24 V input: 40% dimming. (b) BB-FBSRC with 24 V input: 80% dimming. (c) BB-HBSRC with 48 V input: 40% dimming. (d) BB-HBSRC with 48 V input: 80% dimming. (e) HBSRC with 96 V input: 40% dimming. (f) HBSRC with 96 V input: 80% dimming.

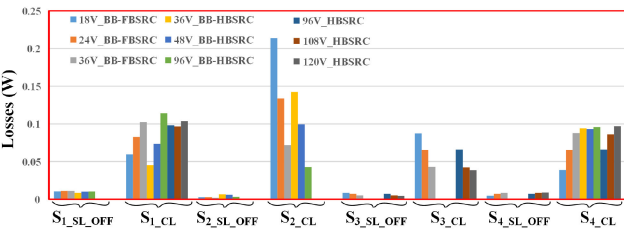


Fig. 25. Simulated loss analysis of proposed configuration under different input voltages in different reconfigurations.

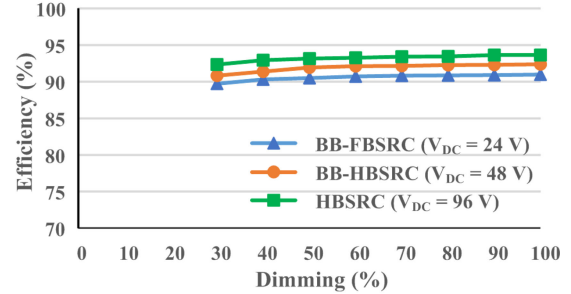
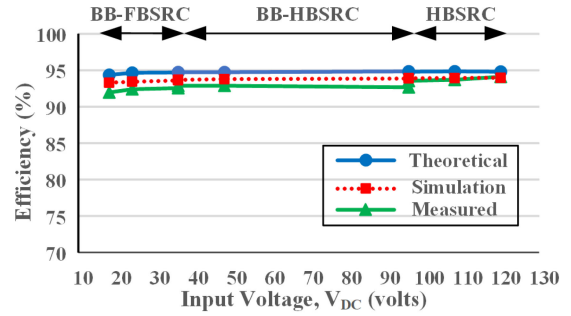


Fig. 26. Efficiency curve with respect to (a) input voltage variations under different reconfigurations and (b) dimming with all the three configurations for 50% duty cycle.

TABLE III
COMPARISON OF WIDE INPUT SOFT-SWITCHED CONVERTERS

Structure	S	D	L	C	T/F	Sec. Win.	Mod.	Rated Power	Input Voltage Range (V)	Range of Switching Frequency	Eff. (%)	Gain Range
Isolated Buck-Boost Converter [14]	8	4	1	4	1	1	PS	380 V/ 800 W	100-400	60 kHz	97.61	0.35-1.4
PWM Resonant Converter [15]	5	1	2	4	1	1	PWM	380 V/ 300 W	25-35	135 kHz	98.9	1.97-2.76
Multilevel LCC Resonant Converter [16]	8	4	1	3	2	1	PWM	5k V/ 100 kW	40-75	50 kHz	-	0.95-2.85
Active Boost Rectifier based Converter [19]	6	0	2	3	1	1	Double Pulse	380 V/ 300 W	25-35	140 kHz	98.61	1.73-2.43
Structure-Reconfigurable Series Resonant Converter [25]	7	3	1	3	1	1	PWM	200 V, 400 V/ 500 W	30-60	100 kHz	95.4	0.5-2
Interleaved Boost+FB LLC [26]	4	2	3	4	1	2	PWM	24 V/ 600 W	120-240	100 kHz	96	0.007-0.014
Buck-boost + HB LLC [27]	4	0	2	3	1	2	PWM	15 V/ 300 W	36-72	100 kHz	93.96	0.8-1.64
Buck-Boost+HB LCC [28]	2	4	3	4	1	1	PWM+PFM	48 V/ 500 W	100-200	98-118 kHz	94	0.432-0.864
4-switch Buck-Boost + FB LLC [29]	6	0	2	3	1	2	PWM	24 V/ 720 W	250-420	1 MHz	96.4	0.116-0.224
Proposed Converter	4	4	2	3	0	0	PWM	22.5 V/ 22 W	18-120	200 kHz	94.19	0.18-1.25

S -No. of Switches, D-No. of Diodes, L-No. of Inductors, C-No. of Capacitors, T/F-No. of Transformers Sec. Win. -No. of Secondary Windings, Mod. - Modulation, Eff. - Efficiency

provides benefits like wider voltage gain and ZVS under wide input variations and, thus, results in reduced switching losses and high efficiency with easier implementation. Also, the proposed configuration is compared with existing wide input soft-switched converters as shown in Table III, where the internal voltage gain of the converters without transformer is compared along with component count, modulation, voltage range, efficiency, etc. It is evident from Table III that the proposed configuration provides various benefits, such as smooth transformation into three different topologies without any additional

switching devices, no topological transitions within a switching cycle in steady state, transformer less, compact in size, soft switching and wider voltage gain with buck/boost operation, and use of simple PI controller in contrast to these topologies.

VII. CONCLUSION

A reconfigurable nonisolated BB-integrated FBSRC-based LED driver is proposed for wide input automotive applications. BB converter operation is integrated with FBSRC and, hence, can be reconfigured as BB-FBSRC, BB-HBSRC, and HBSRC achieving three different levels of voltage gains. APWM technique is employed for voltage regulation. Based on the input voltage range, the converter transforms to one of the three configurations and the corresponding PI controller regulates the output voltage against variations in the input voltage. The proposed converter is analyzed with respect to the design, conduction losses, and voltage and current stress in the devices. The performance has been verified with both simulation and experimental results. It is observed that the proposed configuration smoothly transforms from one configuration to other and can provide voltage regulation with soft switching across the devices in the entire voltage range. Thus, compared with existing LED drivers, the proposed driver provides benefits like wider voltage gain and ZVS under wide input variations and, thus, results in reduced switching losses, easy implementation, and high efficiency under wide input voltages and dimming levels. Also, there are various benefits, such as smoothly transformation into three different topologies without any additional switching devices, no topological transitions within a switching cycle in steady state, transformer less, compact in size, soft switching and wider voltage gain with buck/boost operation, and use of simple PI controller in contrast to the existing wide input soft-switched topologies. Therefore, the proposed LED driver is well suitable for automotive LED lighting applications with wide input voltage variations.

REFERENCES

- [1] A. Mednik, "Automotive LED lighting needs special drivers," *Power Electron. Technol. Mag.*, pp. 22–28, Aug. 2005.
- [2] "TIDA-01167 automotive 12- and 24-V battery input protection reference design," Texas Instruments, 2017. [Online]. Available: <https://www.ti.com/lit/pdf/tiduc41>
- [3] V. Anghel, C. Bartholomeusz, A. G. Vasilica, G. Pristavu, and G. Brezeanu, "Variable off-time control loop for current-mode floating buck converters in LED driving applications," *IEEE J. Solid-State Circuits*, vol. 49, no. 7, pp. 1571–1579, Jul. 2014.
- [4] D. Park, Z. Liu, and H. Lee, "A 40 V 10 W 93%-efficiency current-accuracy-enhanced dimmable LED driver with adaptive timing difference compensation for solid-state lighting applications," *IEEE J. Solid-State Circuits*, vol. 49, no. 8, pp. 1848–1860, Aug. 2014.
- [5] Y. Qin, S. Li, and S. Hui, "Topology-transition control for wide-input-voltage-range efficiency improvement and fast current regulation in automotive LED applications," *IEEE Trans. Ind. Electron.*, vol. 64, no. 7, pp. 5883–5893, Jul. 2017.
- [6] Z. Liu and H. Lee, "A 26 W 97%-efficiency fast-settling dimmable LED driver with dual-nMOS-sensing based glitch-tolerant synchronous current control for high-brightness solid-state lighting applications," *IEEE J. Solid-State Circuits*, vol. 50, no. 9, pp. 2174–2187, Sep. 2015.
- [7] T. Instruments, "Lm3405 1.6 MHz, 1A constant current buck regulator for powering LEDs," LM3405 Data Sheet, Oct. 2016.
- [8] Z. Liu and H. Lee, "A wide-input-range efficiency-enhanced synchronous integrated LED driver with adaptive resonant timing control," *IEEE J. Solid-State Circuits*, vol. 51, no. 8, pp. 1810–1825, Aug. 2016.
- [9] Z. Liu and H. Lee, "A current-accuracy-enhanced wide-input-range DC-DC LED driver with feedforward synchronous current control," *IEEE Trans. Circuits Syst. I: Regular Papers*, vol. 65, no. 11, pp. 3996–4006, Nov. 2018.
- [10] Y. Qu, W. Shu, and J. S. Chang, "A 2.8-MHz 96.1%-peak-efficiency 1.4- μ s-settling-time fully soft-switched LED driver with 0.08–1 dimming range," *IEEE Trans. Power Electron.*, vol. 34, no. 10, pp. 10094–10104, Oct. 2019.
- [11] H. Bi, P. Wang, and Y. Che, "A capacitor clamped H-type boost DC-DC converter with wide voltage-gain range for fuel cell vehicles," *IEEE Trans. Veh. Technol.*, vol. 68, no. 1, pp. 276–290, Jan. 2019.
- [12] Y. Zhang, H. Liu, J. Li, M. Sumner, and C. Xia, "DC-DC boost converter with a wide input range and high voltage gain for fuel cell vehicles," *IEEE Trans. Power Electron.*, vol. 34, no. 5, pp. 4100–4111, May 2019.
- [13] W.-C. Liu, C.-J. Chen, C.-H. Cheng, and H.-J. Chen, "A novel accurate adaptive constant on-time buck converter for a wide-range operation," *IEEE Trans. Power Electron.*, vol. 35, no. 4, pp. 3729–3739, Apr. 2020.
- [14] Y. Li, F. Li, F.-W. Zhao, X.-J. You, K. Zhang, and M. Liang, "Hybrid three-level full-bridge isolated buck-boost converter with clamped inductor for wider voltage range application," *IEEE Trans. Power Electron.*, vol. 34, no. 3, pp. 2923–2937, Mar. 2019.
- [15] J.-W. Kim, M.-H. Park, J.-K. Han, M. Lee, and J.-S. Lai, "PWM resonant converter with asymmetric modulation for ZVS active voltage doubler rectifier and forced half resonance in PV application," *IEEE Trans. Power Electron.*, vol. 35, no. 1, pp. 508–521, Jan. 2020.
- [16] J. A. Martín-Ramos, O. Pardo-Vaquero, J. Díaz, F. Nuño, P. J. Villegas, and A. Martín-Pernía, "Modelling a multilevel LLC resonant AC-DC converter for wide variations in the input and the load," *IEEE Trans. Power Electron.*, vol. 34, no. 6, pp. 5217–5228, Jun. 2019.
- [17] W. Sun, Y. Xing, H. Wu, and J. Ding, "Modified high-efficiency LLC converters with two split resonant branches for wide input-voltage range applications," *IEEE Trans. Power Electron.*, vol. 33, no. 9, pp. 7867–7879, Sep. 2018.
- [18] H. Hu, X. Fang, F. Chen, Z. J. Shen, and I. Batarseh, "A modified high-efficiency LLC converter with two transformers for wide input-voltage range applications," *IEEE Trans. Power Electron.*, vol. 28, no. 4, pp. 1946–1960, Apr. 2013.
- [19] X. Zhao, C.-W. Chen, and J.-S. Lai, "A high-efficiency active-boost-rectifier-based converter with a novel double-pulse duty cycle modulation for PV to DC microgrid applications," *IEEE Trans. Power Electron.*, vol. 34, no. 8, pp. 7462–7473, Aug. 2019.
- [20] M. Xingkui, H. Qisheng, K. Qingbo, X. Yudi, Z. Zhe, and M. A. Andersen, "Grid-connected photovoltaic micro-inverter with new hybrid control LLC resonant converter," in *Proc. IEEE, IECON 42nd Annu. Conf. Ind. Electron. Soc.*, 2016, pp. 2319–2324.
- [21] H. Wu, T. Mu, X. Gao, and Y. Xing, "A secondary-side phase-shift-controlled LLC resonant converter with reduced conduction loss at normal operation for hold-up time compensation application," *IEEE Trans. Power Electron.*, vol. 30, no. 10, pp. 5352–5357, Oct. 2015.
- [22] X. Zhao, L. Zhang, R. Born, and J.-S. Lai, "A high-efficiency hybrid resonant converter with wide-input regulation for photovoltaic applications," *IEEE Trans. Ind. Electron.*, vol. 64, no. 5, pp. 3684–3695, May 2017.
- [23] T. LaBella, W. Yu, J.-S. J. Lai, M. Senesky, and D. Anderson, "A bidirectional-switch-based wide-input range high-efficiency isolated resonant converter for photovoltaic applications," *IEEE Trans. Power Electron.*, vol. 29, no. 7, pp. 3473–3484, Jul. 2014.
- [24] X. Sun, X. Li, Y. Shen, B. Wang, and X. Guo, "Dual-bridge LLC resonant converter with fixed-frequency PWM control for wide input applications," *IEEE Trans. Power Electron.*, vol. 32, no. 1, pp. 69–80, Jan. 2017.
- [25] Y. Shen, H. Wang, A. Al-Durra, Z. Qin, and F. Blaabjerg, "A structure-reconfigurable series resonant DC-DC converter with wide-input and configurable-output voltages," *IEEE Trans. Ind. Appl.*, vol. 55, no. 2, pp. 1752–1764, Mar./Apr. 2019.
- [26] X. Sun, Y. Shen, Y. Zhu, and X. Guo, "Interleaved boost-integrated LLC resonant converter with fixed-frequency PWM control for renewable energy generation applications," *IEEE Trans. Power Electron.*, vol. 30, no. 8, pp. 4312–4326, Aug. 2015.
- [27] Y. Jeong, J.-K. Kim, J.-B. Lee, and G.-W. Moon, "An asymmetric half-bridge resonant converter having a reduced conduction loss for DC/DC power applications with a wide range of low input voltage," *IEEE Trans. Power Electron.*, vol. 32, no. 10, pp. 7795–7804, Oct. 2017.

- [28] L. Lin, J. Xu, Y. Chen, X. Wang, and J. Cao, "Asymmetrical hybrid-controlled half-bridge LCC resonant converter with low conduction loss and wide ZVS operation range," *Electron. Lett.*, vol. 53, no. 21, pp. 1422–1424, 2017.
- [29] Q. Liu, Q. Qian, B. Ren, S. Xu, W. Sun, and L. Yang, "A two-stage buck-boost integrated LLC converter with extended ZVS range and reduced conduction loss for high-frequency and high-efficiency applications," *IEEE J. Emerg. Sel. Top. Power Electron.*, to be published, doi: [10.1109/JESTPE.2019.2956240](https://doi.org/10.1109/JESTPE.2019.2956240).
- [30] C.-C. Hua and Y.-L. Deng, "A novel dual-bridge LLC resonant converter with wide range of low input voltage," *Energy Procedia*, vol. 156, pp. 361–365, 2019.
- [31] R. L. Steigerwald, "A comparison of half-bridge resonant converter topologies," *IEEE Trans. Power Electron.*, vol. 3, no. 2, pp. 174–182, Apr. 1988.
- [32] M. K. Kazmierczuk and D. Czarkowski, *Resonant Power Converters*. Hoboken, NJ, USA: Wiley, 2012.
- [33] "LM3404xx 1-A constant current buck regulator for driving high power LEDs," Texas Instruments, 2015. [Online]. Available: <https://www.ti.com/lit/gpn/lm3404hv>



V. K. Satyakar Veeramallu (Member, IEEE) received the B.Tech. degree in electrical and electronics engineering from Acharya Nagarjuna University, Guntur, India, in 2007, and the M.Tech. degree in power electronics from Jawaharlal Nehru Technological University, Kakinada, India, in 2012. He is working toward the Ph.D. degree with the Department of Electrical Engineering, National Institute of Technology, Warangal, India.

He is presently working with the National Institute of Technology, Andhra Pradesh, India. He is having four years of teaching experience. His research interests include soft-switched nonisolated LED drivers.



S. Porpandiselvi (Member, IEEE) received the B.E. degree in electrical and electronics engineering from Thiagarajar College of Engineering, Madurai, India, in 1996, the M.E. degree in applied electronics from Madurai Kamaraj University, Madurai, India, in 2001, and the Ph.D. degree in electrical engineering from the National Institute of Technology, Warangal, India, in 2014.

Currently, she is working as an Assistant Professor with the Department of Electrical Engineering, National Institute of Technology, Warangal. Her research interests include high frequency inverters for induction heating applications, resonant converters, LED driver circuits, and PV-based applications.



B. L. Narasimharaju (Senior Member, IEEE) was born in Gowribidhanur, Karnataka, India, on May 20, 1975. He received the B.E. and M.E. degrees in electrical engineering from University Visvesvaraya College of Engineering (UVCE), Bangalore, India, in 1999 and 2002, respectively, and the Ph.D. degree from the Indian Institute of Technology Roorkee (IIT Roorkee), Roorkee, India, in 2012.

He worked as Project Trainee with ABB Bangalore, India from March 2001 to August 2001, and since then till March 2002, he worked with LRDE, Ministry of Defence, India. He was a Teaching Assistant with UVCE from 2002 to 2003. From 2003 to 2012, he was a Faculty of Electrical Engineering with Manipal Institute of Technology (MIT), Manipal University, Manipal, India. Currently, he is an Associate Professor with the Department of Electrical Engineering, National Institute of Technology, Warangal, India. His research credential includes, 5 funded research projects worth of 250 Lakhs, 6 Ph.D. guidance, more than 72 research publications of 23 journals, and 49 conference proceedings. His research interests include power conversion and control techniques, LED drivers for lighting systems, bidirectional converter for energy storage integration, multilevel inversion, grid integration of solar energy, switched reluctance motor and induction motor drives, active front end power converters, modulation and soft switching techniques, and AI techniques to control of power converters.

Dr. Narasimharaju is a Life Member of ISTE Delhi and System Society of India (SSI).